

## NEMATIC LIQUIDS IN WEAK CAPILLARY POISEUILLE FLOW: STRUCTURE SCALING LAWS AND EFFECTIVE CONDUCTIVITY IMPLICATIONS

HONG ZHOU AND M. GREGORY FOREST

**Abstract.** We study the scaling properties of heterogeneities in nematic (liquid crystal) polymers that are generated by pressure-driven, capillary Poiseuille flow. These studies complement our earlier drag-driven structure simulations and analyses. We use the mesoscopic Doi-Marrucci-Greco model, which incorporates excluded-volume interactions of the rod-like particle ensemble, distortional elasticity of the dispersion, and hydrodynamic feedback through orientation dependent viscoelastic stresses. The geometry likewise introduces anchoring conditions on the nano-rods which touch the solid boundaries. We first derive flow-orientation steady-state structures for three different anchoring conditions, by asymptotic analysis in the limit of weak pressure gradient. These closed-form expressions yield scaling laws, which predict how lengthscales of distortions in the flow and orientational distribution vary with strength of the excluded volume potential, molecule geometry, and distortional elasticity constants. Next, the asymptotic structures are verified by direct numerical simulations, which provide a high level benchmark on the numerical code and algorithm. Finally, we calculate the effective (thermal or electrical) conductivity tensor of the composite films, and determine scaling behavior of the effective property enhancements generated by capillary Poiseuille flow.

**Key Words.** Liquid crystal (nematic) polymers, asymptotic expansions, partial differential equations, capillary Poiseuille flow, conductivity

### 1. Introduction

The rheological behavior of Poiseuille flow of liquid crystal polymers is of interest for technology applications in processing of high performance fibers and films. Rey and co-workers have studied capillary Poiseuille flows using the Leslie-Ericksen theory for discotic nematic liquid crystals ([4, 5, 6]). Denniston *et al.* have used lattice Boltzmann simulations of Landau-deGennes orientation tensor models to explore the behavior of liquid crystal polymers subject to Poiseuille flow ([9]). In this work we study capillary Poiseuille flow using the Doi-Marrucci-Greco model, which also employs an orientation (second-moment) tensor description of the rod distribution.

We extend our early work ([3], [17]) in the following ways: 1) asymptotic results for tilted anchoring condition are derived; 2) the rotary diffusivity is explicitly coupled in the asymptotic results; 3) direct numerical simulations are carried out to validate asymptotic results; and 4) effective conductivity properties of Poiseuille flow-generated composite films are calculated.

The paper is organized as follows. First, we describe the model of liquid crystal polymer hydrodynamics proposed by Doi, Marrucci and Greco ([10, 25, 26, 27]). Second, we present the structure scaling properties of the orientation tensor for different anchoring conditions; this is achieved by asymptotic analysis that yields exact orientation modes with spatial variations controlled by material and boundary conditions in the limit of weak pressure gradient. We perform direct numerical simulations to verify the asymptotic results, and then observe new properties as the asymptotic conditions are violated. Finally, we calculate the effective (thermal or electrical) conductivity tensor of the composite films, and determine scaling behavior of the effective property enhancements generated by capillary Poiseuille flow.

## 2. Model Formulation

We consider capillary Poiseuille flow of nematic liquid crystal polymers (LCPs). Capillary Poiseuille flow is the flow between two non-slip boundaries at  $y = -h$  and  $y = h$  driven by a pressure gradient in this context. The flow is described by a velocity field  $\mathbf{v} = (v_x(y, t), 0, 0)$  with the centerline of the pipe located at  $y = 0$ . Figure 1 depicts the cross-section of the Poiseuille flow on the  $(x, y)$  plane. For simplicity here we suppress variations in the direction of flow ( $x$ ) and primary vorticity direction ( $z$ ), and transport in the vertical ( $y$ ) direction.

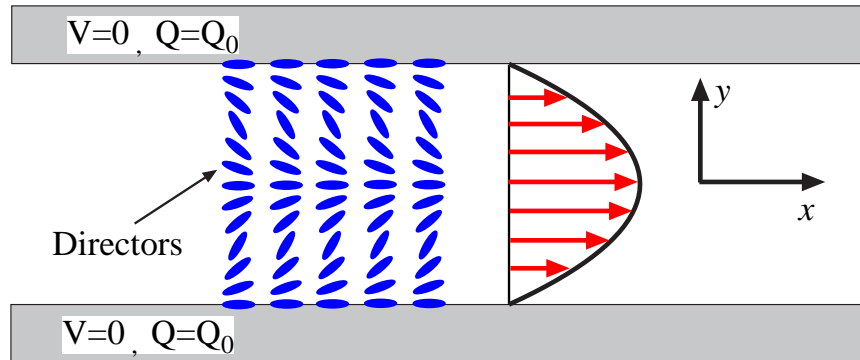


FIGURE 1. Plane Poiseuille flow geometry. Non-slip boundary conditions for the velocity and boundary anchoring for the orientation tensor given by the stable nematic rest state are prescribed, with major director angle  $\psi_0 = 0$  shown here.

The dimensionless governing equations consist of the balance of linear momentum, stress constitutive equation, continuity equation, and the equation for the

orientation tensor ([17]):

$$\begin{aligned}
\frac{d\mathbf{v}}{dt} &= \nabla \cdot (-p\mathbf{I} + \boldsymbol{\tau}), \quad p = \epsilon x, \\
\boldsymbol{\tau} &= \left(\frac{2}{Re} + \mu_3\right)\mathbf{D} + a\alpha F(\mathbf{Q}) \\
&\quad + \frac{a\alpha}{3Er} \left\{ \Delta\mathbf{Q} : \mathbf{Q}(\mathbf{Q} + \frac{\mathbf{I}}{3}) - \frac{1}{2}(\Delta\mathbf{Q}\mathbf{Q} + \mathbf{Q}\Delta\mathbf{Q}) - \frac{1}{3}\Delta\mathbf{Q} \right\} \\
&\quad + \frac{\alpha}{3Er} \left\{ \frac{1}{2}(\mathbf{Q}\Delta\mathbf{Q} - \Delta\mathbf{Q}\mathbf{Q}) - \frac{1}{4}(\nabla\mathbf{Q} : \nabla\mathbf{Q} - \nabla\nabla\mathbf{Q} : \mathbf{Q}) \right\} \\
(1) \quad &\quad + \mu_1 \left\{ (\mathbf{Q} + \frac{\mathbf{I}}{3})\mathbf{D} + \mathbf{D}(\mathbf{Q} + \frac{\mathbf{I}}{3}) \right\} + \mu_2\mathbf{D} : \mathbf{Q} \left( \mathbf{Q} + \frac{\mathbf{I}}{3} \right),
\end{aligned}$$

$$\nabla \cdot \mathbf{v} = 0,$$

$$\begin{aligned}
\frac{d}{dt}\mathbf{Q} &= \boldsymbol{\Omega}\mathbf{Q} - \mathbf{Q}\boldsymbol{\Omega} + a[\mathbf{D}\mathbf{Q} + \mathbf{Q}\mathbf{D}] + \frac{2a}{3}\mathbf{D} - 2a\mathbf{D} : \mathbf{Q}(\mathbf{Q} + \frac{\mathbf{I}}{3}) \\
&\quad - \frac{1}{\Lambda} \left\{ F(\mathbf{Q}) + \frac{1}{3Er} [\Delta\mathbf{Q} : \mathbf{Q}(\mathbf{Q} + \frac{\mathbf{I}}{3}) - \frac{1}{2}(\Delta\mathbf{Q}\mathbf{Q} + \mathbf{Q}\Delta\mathbf{Q}) - \frac{1}{3}\Delta\mathbf{Q}] \right\},
\end{aligned}$$

where  $\mathbf{v}$  is the velocity field for the flowing LCP,  $p$  is the pressure,  $\mathbf{I}$  is the unit tensor,  $\boldsymbol{\tau}$  is the total stress,  $a$  is a dimensionless parameter depending on the molecular aspect ratio  $r$  of spheroidal molecules

$$a = \frac{r^2 - 1}{r^2 + 1},$$

$Re$  is the solvent Reynolds number,  $Er$  is the Ericksen number which is a reciprocal elasticity constant,  $\mu_i$  ( $i = 1, 2, 3$ ) are three nematic Reynolds numbers,  $\alpha$  is a normalized entropic parameter,  $\mathbf{D}$  is the rate-of-strain tensor and  $\boldsymbol{\Omega}$  is the vorticity tensor,

$$(2) \quad \mathbf{D} = \frac{1}{2}(\nabla\mathbf{v} + \nabla\mathbf{v}^T), \quad \boldsymbol{\Omega} = \frac{1}{2}(\nabla\mathbf{v} - \nabla\mathbf{v}^T).$$

Here the superscript  $T$  denotes the transpose of a second order tensor.

$$(3) \quad F(\mathbf{Q}) = (1 - N/3)\mathbf{Q} - N\mathbf{Q}^2 + N\mathbf{Q} : \mathbf{Q}(\mathbf{Q} + \mathbf{I}/3),$$

$$(4) \quad \Lambda = \begin{cases} 1, & \text{with constant rotary diffusivity,} \\ (1 - \frac{3}{2}\mathbf{Q} : \mathbf{Q})^2, & \text{with orientation-dependent rotary diffusivity.} \end{cases}$$

The no slip condition at the bounding surfaces is used for the scaled axial velocity  $v_x$ :

$$(5) \quad v_x|_{y=\pm 1} = 0.$$

Homogeneous mesophase anchoring is assumed at the boundaries, which assumes that the rod ensemble is in an equilibrium bulk phase. We work at a concentration where the rest state is a stable ordered equilibrium, called the nematic phase:

$$\begin{aligned}
(6) \quad \mathbf{Q}|_{y=\pm 1} &= s_0(\mathbf{nn} - \frac{\mathbf{I}}{3}), \\
s_0 &= \frac{1}{4}(1 + 3\sqrt{1 - \frac{8}{3N}}),
\end{aligned}$$

where  $s_0$  is the stable uniaxial order parameter specified by the nematic concentration  $N > \frac{8}{3}$ , and  $\mathbf{n}$  is the equilibrium uniaxial director. We will fix  $N > 3$  so

that the nematic phase is the unique stable equilibrium, limiting the chances of potential hysteresis and bi-stability in flow-induced structures. We assume  $\mathbf{n}$  lies in the flow-flow gradient plane at some experimentally dictated *anchoring angle*  $\psi_0$  with respect to the flow direction,

$$(7) \quad \mathbf{n} = (\cos \psi_0, \sin \psi_0, 0).$$

$\psi_0 = 0$ ,  $\psi_0 = \frac{\pi}{2}$ , and  $0 < \psi_0 < \frac{\pi}{2}$  correspond to tangential, homeotropic and tilted anchoring, respectively.

We consider the in-plane mesophase orientation of LCPs with two directors of  $\mathbf{Q}$  confined to the plane  $(x, y)$ , but still admitting biaxiality. This restriction is not easily lifted for the analysis to follow; numerically, there is not limitation. The point, however, is to glean some prediction of the types of spatial structures that arise, out of equilibrium phases, due to the combined influences of a pressure gradient induced flow, and anchoring of the rod ensemble at the walls. We will find, consistent with our earlier analyses, two types of structure modes: extended structures in the orientational distribution which accompany the Poiseuille flow geometry; and, boundary layers which arise due to wall confinement. Drilling somewhat deeper in these analytical, though asymptotic, insights into structures, a more important question is a prediction of the *scaling laws* of each type of structure mode. Namely, it is impossible to explore this multi-parameter space even with large-scale computations; guidance as to how the lengthscales of spatial heterogeneity vary with parameters is of paramount value in guiding our subsequent numerical simulations. Thus, we make no apologies either for the reduction in physical space dimensions from three to one, or for the reduction in orientational degrees of freedom, namely from a full probability distribution function with infinite degrees of freedom to a second-moment tensor with generally five degrees of freedom, and now to a second-moment whose peak axis of orientation must lie in the plane of the primary flow and flow-gradient directions. These assumptions shall lead to explicit structure modes and scaling laws, in flow and particle orientation, as well as an indication of when these asymptotic approximations will break down. Those insights will then indicate grid-scale resolution of algorithms across parameter space.

The in-plane orientational constraint implies that two components in the Cartesian representation of  $\mathbf{Q}$  must vanish,  $Q_{xz} = Q_{yz} = 0$ . Alternatively, the orientation tensor can be written in terms of directors and order parameters:

$$(8) \quad \mathbf{Q} = s(y, t)(\mathbf{nn} - \frac{\mathbf{I}}{3}) + \beta(y, t)(\mathbf{n}^\perp \mathbf{n}^\perp - \frac{\mathbf{I}}{3}),$$

with the directors  $\mathbf{n}, \mathbf{n}^\perp$  confined to the  $(x, y)$  plane and parametrized by the in-plane Leslie angle  $\psi(y, t)$ ,

$$(9) \quad \mathbf{n} = (\cos \psi, \sin \psi, 0), \mathbf{n}^\perp = (-\sin \psi, \cos \psi, 0).$$

The third director is rigidly constrained along the vorticity axis.

The explicit coordinate change between these  $\mathbf{Q}$  representations is:

$$(10) \quad \begin{aligned} Q_{xx} &= s(\cos^2 \psi - \frac{1}{3}) + \beta(\sin^2 \psi - \frac{1}{3}), \\ Q_{xy} &= (s - \beta) \sin \psi \cos \psi, \\ Q_{yy} &= s(\sin^2 \psi - \frac{1}{3}) + \beta(\cos^2 \psi - \frac{1}{3}). \end{aligned}$$

With the biaxial representation (8) of  $\mathbf{Q}$ , the tensor equation in (5) can be written explicitly in terms of the two order parameters  $(s, \beta)$  and the Leslie angle  $\psi$ :

$$\begin{aligned}
 \frac{\partial s}{\partial t} &= -\frac{1}{\Lambda} \left\{ U(s) + \frac{2N}{3}s\beta(1 + \beta - s) + \frac{2}{9Er}(s - \beta)g(s, \beta) \left(\frac{\partial \psi}{\partial y}\right)^2 \right. \\
 &\quad \left. + \frac{1}{9Er} \left[ -(1-s)(1-\beta+2s) \frac{\partial^2 s}{\partial y^2} + s(1-s+2\beta) \frac{\partial^2 \beta}{\partial y^2} \right] \right\} \\
 &\quad + \frac{a}{3} \frac{\partial v_x}{\partial y} g(s, \beta) \sin 2\psi, \\
 \frac{\partial \beta}{\partial t} &= -\frac{1}{\Lambda} \left\{ U(\beta) + \frac{2N}{3}s\beta(1 + s - \beta) + \frac{2}{9Er}(\beta - s)g(\beta, s) \left(\frac{\partial \psi}{\partial y}\right)^2 \right. \\
 (11) \quad &\quad \left. + \frac{1}{9Er} \left[ \beta(1-\beta+2s) \frac{\partial^2 s}{\partial y^2} - (1-\beta)(1-s+2\beta) \frac{\partial^2 \beta}{\partial y^2} \right] \right\} \\
 &\quad - \frac{a}{3} \frac{\partial v_x}{\partial y} g(\beta, s) \sin 2\psi, \\
 \frac{\partial \psi}{\partial t} &= \frac{1}{6(s-\beta)} \left\{ \frac{\partial v_x}{\partial y} (3\beta - 3s + a(2 + s + \beta) \cos 2\psi) \right. \\
 &\quad \left. + \frac{1}{3Er\Lambda} (2 + s + \beta) \left[ (s - \beta) \frac{\partial^2 \psi}{\partial y^2} + 2 \frac{\partial \psi}{\partial y} \left( \frac{\partial s}{\partial y} - \frac{\partial \beta}{\partial y} \right) \right] \right\},
 \end{aligned}$$

where

$$\begin{aligned}
 (12) \quad U(s) &= s \left( 1 - \frac{N}{3}(1-s)(2s+1) \right), \\
 g(s, \beta) &= 1 + 3s\beta - \beta + 2s - 3s^2.
 \end{aligned}$$

The momentum equation is reduced to a single equation for the axial velocity component  $v_x$ ,

$$\begin{aligned}
 \frac{\partial v_x}{\partial t} &= \frac{\partial \tau_{xy}}{\partial y} - \epsilon, \\
 \tau_{xy} &= \frac{a\alpha}{2} \left[ U(s) - U(\beta) + \frac{4Ns\beta}{3}(\beta - s) \right] \sin 2\psi \\
 &\quad + \frac{a\alpha}{18Er} \left[ -h(s, \beta) \frac{\partial^2 s}{\partial y^2} + h(\beta, s) \frac{\partial^2 \beta}{\partial y^2} + 2(s - \beta)\gamma(s, \beta) \left(\frac{\partial \psi}{\partial y}\right)^2 \right] \sin 2\psi \\
 (13) \quad &\quad + \frac{a\alpha}{18Er} (s + \beta + 2) \left[ (\beta - s) \frac{\partial^2 \psi}{\partial y^2} - 2 \left( \frac{\partial s}{\partial y} - \frac{\partial \beta}{\partial y} \right) \frac{\partial \psi}{\partial y} \right] \cos 2\psi \\
 &\quad + \frac{\alpha}{6Er} (s - \beta) \left[ (s - \beta) \frac{\partial^2 \psi}{\partial y^2} + 2 \left( \frac{\partial s}{\partial y} - \frac{\partial \beta}{\partial y} \right) \frac{\partial \psi}{\partial y} \right] \\
 &\quad + \left[ \frac{\mu_1}{6} (s + \beta + 2) + \frac{\mu_2}{8} (s - \beta)^2 (1 - \cos 4\psi) + \frac{1}{Re} + \frac{\mu_3}{2} \right] \frac{\partial v_x}{\partial y},
 \end{aligned}$$

where

$$\begin{aligned}
 (14) \quad \gamma(s, \beta) &= g(s, \beta) + g(\beta, s), \\
 h(s, \beta) &= (1 - \beta + 2s)(1 + \beta - s).
 \end{aligned}$$

We seek steady solutions of the dimensionless governing equations (11-14) subject to the boundary conditions

$$(15) \quad v_x|_{y=\pm 1} = 0, \quad s|_{y=\pm 1} = s_0, \quad \beta|_{y=\pm 1} = 0, \quad \psi|_{y=\pm 1} = \psi_0.$$

We posit a formal asymptotic expansion in the small  $\epsilon$  limit, consistent with the above boundary conditions:

$$\begin{aligned}
 (16) \quad v_x &= \sum_{k=1}^{\infty} v_x^{(k)}(y)\epsilon^k, \quad \psi = \sum_{k=0}^{\infty} \psi^{(k)}(y)\epsilon^k, \\
 s &= \sum_{k=0}^{\infty} s^{(k)}(y)\epsilon^k, \quad \beta = \sum_{k=1}^{\infty} \beta^{(k)}(y)\epsilon^k.
 \end{aligned}$$

Alternatively, the Cartesian representation of  $\mathbf{Q}$  is expanded in the form:

$$(17) \quad \mathbf{Q} = \sum_{k=0}^{\infty} \mathbf{Q}^{(k)}(y)\epsilon^k,$$

with  $\mathbf{Q}^{(0)}$  a quiescent, homogeneous equilibrium given by (6).  $\psi^{(1)}$ ,  $s^{(1)}$ ,  $\beta^{(1)}$  and the components of  $\mathbf{Q}^{(1)}$  are explicitly related by :

$$\begin{aligned}
 (18) \quad \psi^{(1)} &= \frac{2Q_{xy}^{(1)} \cos 2\psi_0 - (Q_{xx}^{(1)} - Q_{yy}^{(1)}) \sin 2\psi_0}{2s}, \\
 s^{(1)} &= \frac{3}{2}(Q_{xx}^{(1)} + Q_{yy}^{(1)}) + \frac{1}{2}(Q_{xx}^{(1)} - Q_{yy}^{(1)}) \cos 2\psi_0 + Q_{xy}^{(1)} \sin 2\psi_0, \\
 \beta^{(1)} &= \frac{3}{2}(Q_{xx}^{(1)} + Q_{yy}^{(1)}) - \frac{1}{2}(Q_{xx}^{(1)} - Q_{yy}^{(1)}) \cos 2\psi_0 - Q_{xy}^{(1)} \sin 2\psi_0.
 \end{aligned}$$

We remark that anchoring conditions at the two boundaries are assumed identical. Different conditions at each boundary require a non-homogeneous steady structure at leading order ([34]), which we will not pursue for this study.

### 3. Steady Asymptotic Structures

From either representation of  $\mathbf{Q}$ , the above expansions are inserted into the full system of flow-nematic equations, (1)-(4) or (11)-(12), equations for the  $O(\epsilon)$  and  $O(\epsilon^2)$  variables derived, and then systematically solved. We now state the results, following the notation in expansion (16).

**3.1. Velocity Structure.** The axial velocity at  $O(\epsilon)$ ,  $v_x^{(1)}$ , reproduces the simple Poiseuille flow structure:

$$(19) \quad v_x^{(1)} = C_v (1 - y^2),$$

where

$$\begin{aligned}
 C_v &= \frac{3}{\frac{6}{Re} + \mu_1(2 + s_0) + 3\mu_3 + \frac{3}{2}\mu_2 s_0^2 \sin^2(2\psi_0) + (M_1 M_2 + M_3)\alpha}, \\
 M_1 &= \frac{3\Lambda}{2 + s_0}(1 - \lambda_L \cos 2\psi_0), \\
 (20) \quad M_2 &= 3s_0^2(1 - \lambda_L \cos 2\psi_0), \\
 M_3 &= a^2 \sin^2(2\psi_0) \Lambda(2 + s_0 - 3s_0^2), \\
 \lambda_L &= \frac{a(2 + s_0)}{3s_0}.
 \end{aligned}$$

**3.2. Director Structure.** The first consequence of these exact mesoscopic solutions is quite striking: *the director is seen to only participate in the long-range extended structure and to not vary in the boundary layers.* From equation (18), the director angle  $\psi$  is explicitly given by

$$(21) \quad \psi = \psi_0 + \epsilon C_p y(1 - y^2) + O(\epsilon^2), \quad C_p = C_v M_1 Er.$$

By inference, the confinement-induced boundary layer structures are therefore responsible only for focusing of the orientational distribution.

It is easy to show that  $M_1 M_2 + M_3 > 0$ . Then, in the denominator of  $C_v$ , all terms are positive definite, so that  $C_v$  is positive definite.  $M_1$ , however, is not: it depends on whether the Leslie parameter  $\lambda_L$  is greater or less than one. As in Couette (plate-driven) flow ([17]), this controls the direction of twist of the major director from plate to plate, from formula (21).

**3.3. Order Parameter Structure.** We now extract degree and scales of molecular elasticity induced by slow Poiseuille flow. The striking feature is extreme sensitivity to anchoring angle. From the  $s, \beta$  formulas, (18), it follows that  $s^{(1)}$  and  $\beta^{(1)}$  *vanish* if and only if  $\psi_0 = 0, \frac{\pi}{2} \pmod{\pi}$ . These were the sole boundary conditions considered in ([3]), so the tilted structures presented here will have different features, again matching the similar phenomenon discovered in Couette flow ([17]).

- *Tangential anchoring* ( $\psi_0 = 0$ )

Order parameter distortions enter at  $O(\epsilon^2)$  through two boundary layers and the long-range permeation structure:

$$\begin{aligned}
 (22) \quad s &= s_0 + \epsilon^2 s^{(2)} + O(\epsilon^3), \\
 \beta &= \epsilon^2 \beta^{(2)} + O(\epsilon^3), \\
 \beta^{(2)} &= C_1^{(2)} \cosh(Er^{1/2} G y) + A_2^{(2)} y^4 + C_2^{(2)} y^2 + E_2^{(2)}, \\
 s^{(2)} &= 2C_3^{(2)} \cosh(Er^{1/2} H y) + 2C_5^{(2)} \cosh(Er^{1/2} G y) \\
 &\quad + C_7^{(2)} y^4 + C_9^{(2)} y^2 + C_{11}^{(2)},
 \end{aligned}$$

where

$$\begin{aligned}
 G &= \sqrt{\frac{9 - 3N + 6Ns_0^2 + 6Ns_0}{1 - s_0}}, & H &= \sqrt{\frac{9 - 3N + 18Ns_0^2 - 6Ns_0}{1 + s_0 - 2s_0^2}}, \\
 A_2^{(2)} &= \frac{2C_p(1 - s_0)(3s_0C_p - 2aC_vEr\Lambda \cos 2\psi_0)}{Er(3 - N + 2Ns_0^2 + 2Ns_0)}, \\
 C_2^{(2)} &= \frac{12(A_2^{(2)} - C_p^2s_0 + aC_vC_pEr\Lambda \cos 2\psi_0)}{ErG^2}, \\
 E_2^{(2)} &= \frac{2(C_2^{(2)} + C_p^2s_0)}{ErG^2}, & C_1^{(2)} &= -\frac{A_2^{(2)} + C_2^{(2)} + E_2^{(2)}}{\cosh(Er^{1/2}G)}, \\
 C_5^{(2)} &= \frac{s_0(G^2 + 6N)C_1^{(2)}}{(1 + 2s_0)(G^2 - H^2)}, \\
 C_7^{(2)} &= -\frac{6[ErNs_0A_2^{(2)} + C_p(3s_0 + 1)(3s_0C_p - 2aC_vEr\Lambda \cos 2\psi_0)]}{ErH^2(1 + 2s_0)}, \\
 C_9^{(2)} &= \frac{6}{ErH^2(1 + 2s_0)}[2(1 + 2s_0)C_7^{(2)} - s_0(2A_2^{(2)} + ErNC_2^{(2)}) \\
 &\quad + 2C_p(1 + 3s_0)(C_p s_0 - aC_vEr\Lambda \cos 2\psi_0)], \\
 C_{11}^{(2)} &= \frac{2(1 + 2s_0)C_9^{(2)} - 2s_0(2C_2^{(2)} + 3ErNC_2^{(2)}) - 2C_p^2s_0(1 + 3s_0)}{ErH^2(1 + 2s_0)}, \\
 C_3^{(2)} &= -\frac{2C_5^{(2)} \cosh(Er^{1/2}G) + C_7^{(2)} + C_9^{(2)} + C_{11}^{(2)}}{2 \cosh(Er^{1/2}H)}.
 \end{aligned}$$

Combined with the director results, (21), we conclude that tangential anchoring leads to a director-dominated, non-uniform, long-range structure with  $Er^{-1}$  mean scaling, the same behavior as in Couette flow. This implies that pressure-driven and drag-driven flows, which are respectively parabolic and linear shear layers, do not alter the molecular elasticity-dominated orientational gradients.

- *Normal (homeotropic) anchoring* ( $\psi_0 = \pi/2$ )

The structure model (11)-(15) for in-plane  $\mathbf{Q}$  tensors admits a symmetry:  $(a, \psi) \rightarrow (-a, \frac{\pi}{2} + \psi)$ . This property implies the asymptotic solution with  $\psi_0 = \pi/2$  can be obtained directly from (22). *Thus normal and tangential anchoring structures are quantitatively different, with changes in numerical pre-factors, yet have qualitatively similar scaling laws.* The figures will illustrate these features.

- *Tilted anchoring* ( $0 < \psi_0 < \pi/2$  or  $\pi/2 < \psi_0 < \pi$ )

Any pre-tilt induces an order parameter response of the same amplitude,  $O(\epsilon)$ , as the director distortion, yet localized in the two boundary layers:

$$\begin{aligned}
 (23) \quad s &= s_0 + \epsilon s^{(1)} + O(\epsilon^2), \\
 \beta &= \epsilon \beta^{(1)} + O(\epsilon^2),
 \end{aligned}$$

where

$$\beta^{(1)} = 2 A_1 \sinh(Er^{1/2} D y) + A_2 y,$$

$$s^{(1)} = 2 C_1 \sinh(Er^{1/2} F y) - C_2 y + 2 C_3 \sinh(Er^{1/2} D y),$$

$$B = 9 + 6N s_0 - 3N + 6N s_0^2, \quad D = \sqrt{\frac{B}{1 - s_0}},$$

$$A_2 = \frac{6aC_v \Lambda \sin(2\psi_0) (1 - s_0)}{B}, \quad A_1 = -\frac{A_2}{2 \sinh(Er^{1/2} D)},$$

$$B_1 = 18N s_0^2 - 3N - 6N s_0 + 9, \quad B_2 = 6aC_v \Lambda \sin(2\psi_0) (1 + 2s_0 - 3s_0^2),$$

$$B_3 = \frac{6N s_0 (1 - s_0) A_2 + B_2}{B_1},$$

$$F = \sqrt{\frac{B_1}{1 + s_0 - 2s_0^2}}, \quad C_2 = \frac{6N s_0 (1 - s_0) A_2 + B_2}{B_1},$$

$$C_3 = \frac{(s_0 - s_0^2) A_1 (Er D^2 + 6Er N)}{(1 + s_0 - 2s_0^2 - B_1 Er) Er D^2},$$

$$C_1 = \frac{B_3 - 2C_3 \sinh(Er^{1/2} D)}{2 \sinh(Er^{1/2} F)}.$$

This result for Poiseuille flow is qualitatively similar to Couette flow in the slow flow limit ([3], [17]). It suggests a flow-nematic structure mechanism: molecular elasticity is amplified in local boundary layers when the major director is pinned at an angle tilted with respect to the flow-flow gradient axes. This result forebodes a phenomenon that only occurs at much higher driving conditions or with much "softer" elasticity constants, namely the appearance of defects in the orientational distribution. These structures correspond to local regions of isotropy (randomness) of the orientational distribution. In such regions, the local principal axes of orientation are not able to align with the primary flow axes, which causes sharp boundary layers with even smaller lengthscales, on the order of  $Er^{-\frac{1}{2}}$  according to the predictions above. Since  $Er$  for nematic polymers are on the order of  $10^6$ , this suggests a very stringent grid-scale will be required to resolve these structures, and, an adaptive mesh refinement technique will be required since there is no *a priori* knowledge of where these defects will arise. Finally, in nematic polymers as opposed to liquid crystals, defects are transient as opposed to preserved, and attractors are dynamic rather than predominantly steady; this means under-resolution in time integrators or simply a focus on steady structures are essentially useless.

#### 4. Effective Conductivity Tensors

We now take the results from above on pressure-driven processing flows, and predict what kinds of conductivity features are associated with these orientational distributions. This is part of an effort within our larger research group to link processing of nematic polymer nano-composites (NPNCs) to effective properties. In ([32]), we developed a connection between the probability distribution function of nematic polymers and the effective conductivity tensor of low-volume-fraction

nanocomposite materials based on homogenization theory. One simply needs to posit the properties of the nano-rods and of the matrix, where each phase is assumed to be an isotropic material. Extensions to anisotropic nano and matrix phases are straightforward, but a detail that only clouds the essential predictions we wish to convey here.

This approach considers spheroidal molecules (rods in this instance) with molecular orientation  $\mathbf{m}$ , aspect ratio  $r$ , isotropic conductivity  $\sigma_2$  and volume fraction  $\theta_2$  (assumed quite small, indeed in practical nano-composites on the order of 1%) populated in a matrix of conductivity  $\sigma_1$  according to the orientation distribution function  $f(\mathbf{m})$  of the ensemble. Conductivity obeys elliptic equations which are virtually identical for thermal, electric, and dielectric properties. The volume fraction,  $\theta_2$ , of the nematic polymer inclusions is proportional to the dimensionless strength,  $N$ , of the Maier-Saupe excluded volume potential:

$$(24) \quad \theta_2 = \frac{N\pi}{8r},$$

where  $r = l/d$  is the aspect ratio of the molecular spheroids with length  $l$  and diameter  $d$ . Then, the effective conductivity tensor in closed form is derived in the low-volume-fraction limit ( $\theta_2 \ll 1$ ) as:

$$(25) \quad \sigma^e = \sigma_1 \mathbf{I} + \sigma_1 \theta_2 (\sigma_2 - \sigma_1) \left\{ \frac{2}{\sigma_2 + \sigma_1 - (\sigma_2 - \sigma_1)L_a} \mathbf{I} + \frac{(\sigma_2 - \sigma_1)(1 - 3L_a)}{[(\sigma_2 + \sigma_1) - (\sigma_2 - \sigma_1)L_a][\sigma_1 + ((\sigma_2 - \sigma_1)L_a)]} \mathbf{M}(f) \right\} + O(\theta_2^2),$$

where  $\mathbf{I}$  is the 3 by 3 identity matrix,  $L_a$  is the spheroidal depolarization factor depending on the nematogen aspect ratio  $r$  through the relation

$$(26) \quad L_a = \frac{1 - \epsilon^2}{\epsilon^2} \left[ \frac{1}{2\epsilon} \ln \left( \frac{1 + \epsilon}{1 - \epsilon} \right) - 1 \right], \quad \epsilon = \sqrt{1 - r^{-2}}.$$

Here the orientation probability distribution function of the LCP inclusions,  $f$ , is governed by the Smoluchowski equation of the Doi-Hess kinetic theory for quiescent or flowing nematic polymers ([18]);  $\mathbf{M}(f)$  is the second-moment of the orientation probability density  $f$ . Recall that the orientation tensor  $\mathbf{Q}$  of the previous development is simply  $\mathbf{Q} = \mathbf{M} - \frac{1}{3}\mathbf{I}$ .

From equation (25) it is obvious that the effective conductivity shares the same three principal axes with the second moment tensor  $\mathbf{M}(f)$ . We denote the three principle values of conductivity (i.e. eigenvalues of  $\sigma^e$ ) as  $\sigma_1^e \geq \sigma_2^e \geq \sigma_3^e$ , where the largest principal value,  $\sigma_1^e$ , is the maximum effective conductivity. The relative principal value enhancements are given by

$$(27) \quad \varepsilon_i = \frac{\sigma_i^e - \sigma_1}{\sigma_1}, \quad i = 1, 2, 3,$$

where  $\varepsilon_1 \geq \varepsilon_2 \geq \varepsilon_3$ . The value  $\varepsilon_1 - \varepsilon_2$  depicts property anisotropy with respect to the two principal conductivity directions, whereas  $\varepsilon_1$  captures the maximum scalar enhancement due to the nematic polymer inclusions. For example,  $\varepsilon_1 = 1$  implies  $\sigma_1^e = 2\sigma_1$  or 100% gain of the bulk composite conductivity.

Heterogeneous effective properties of sheared and extension-enhanced nematic polymer nanocomposites have been studied in ([18, 33]). In the next section we will study the anisotropy and effective properties enhanced by Poiseuille flows.

## 5. Numerical Results

**5.1. Numerical Methods.** In order to numerically find the steady state solutions of the boundary value problem (11-15), we use Newton's method to iteratively obtain the steady state solutions. Our codes cannot resolve parameter regimes where  $Er$  is above a critical threshold value; this may be either due to singular structures or due to structure transitions where steady structures give rise to transient attractors. In the high Ericksen number limit, where the lengthscales of distortional elasticity are predicted to scale like  $Er^{-1}$  and  $Er^{-1/2}$ , adaptive gridding will be required since one does not know *a priori* where these internal boundary layers will form. Some of these numerical tools have been developed in our group, but none have yet been applied to pressure-driven flows.

**5.2. Numerical validation of the asymptotic results and vice versa.** Figures 2-4 compare the exact asymptotic formulas for the director angle  $\psi$ , order parameters  $s$ ,  $\beta$ , and flow velocity  $v_x$ , with direct numerical solutions of the steady, boundary value problem. Figure 4 also gives shear stress and light scattering intensity predictions, which provide a basis for experimental validation. For the computations shown here, we fix a concentration in the nematic regime  $N = 6$  and the aspect ratio  $r = 3$  (i.e.,  $a = 0.8$ ), consistent with our earlier studies ([14, 17]).

We begin with confirmation of the formulas for  $0 < \epsilon \ll 1$  and  $0 < \epsilon \cdot Er \ll 1$ , Figure 2, where the asymptotic formulas are nearly identical to the numerical solutions. For tangential and normal anchoring, we set  $\epsilon = 0.1$ ,  $Er = 1$ ; for tilted anchoring,  $\psi_0 = \frac{\pi}{6}$ , we have to lower  $\epsilon = 0.05$  with the same  $Er = 1$  to maintain agreement between the asymptotic formulas and the numerical solutions.

Next we illustrate breakdown of the asymptotic formulas with direct numerical solutions when either of the two asymptotic conditions,  $\epsilon \ll 1$  and  $\epsilon \cdot Er \ll 1$ , are gradually pushed out of the asymptotic regime. Our purpose here is to monitor emergence of new, non-asymptotic structures, and to identify sources of additional scaling behavior.

Figure 3 imposes tangential (Figure 3c and d) and normal anchoring (Figure 3e and f) with  $\epsilon = 0.3$ ,  $Er = 10$ . For tilted anchoring, Figures 3a, 3b, a more stringent  $\epsilon \cdot Er$  condition is needed for asymptotic agreement, with  $\epsilon = 0.5$ ,  $Er = 1$ . One finds quantitative asymptotic accuracy.

In Figure 4a,b, we raise the pressure gradient to ( $\epsilon = 0.5$ ), with  $Er = 20$  (for which  $\epsilon \cdot Er = 10$ ), and present results only with normal anchoring. Note that the velocity profile departs from being parabolic near the boundaries. The concavity of the velocity profile changes from concave-up to concave-down and then concave-up again. We further give predictions of shear-gap stresses (Figure 4c) and light intensity patterns (Figure 4d) associated with these steady structures. Neither  $N_1$  nor  $N_2$  changes sign across the rectangular pipe. The light scattering intensity across the pipe associated with the numerical solutions is given in Figure 4d. This intensity pattern can be viewed as a combination of pure nematic patterns of the Doi-Marrucci-Greco theory, ([15, 16]), where the flow coupling has led to selection of order-parameter structures near the plates and director structures in the interior.

**5.3. Effective conductivity properties.** Our main focus in this subsection is the determination of effective properties associated with capillary Poiseuille flow. We consider typical model NPNCs with the nanorod aspect ratio  $r = 100$  (and one with  $r = 3$  for comparison) and the conductivity contrast between the matrix solvent and nanophase as  $\sigma_1/\sigma_2 = 10^{-5}$ . This ratio is, in fact, quite modest; some composites have contrasts of ten or greater orders of magnitude. Figure 5

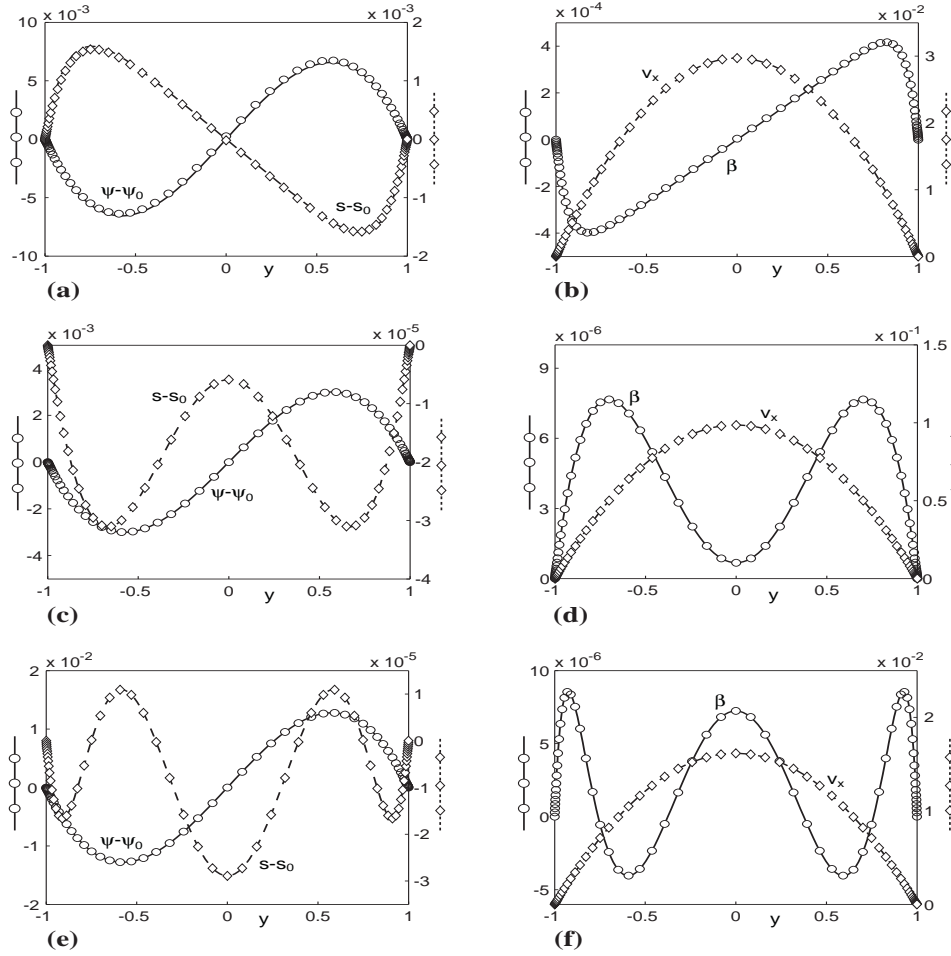


FIGURE 2. Comparison of the numerical solutions (circles or triangles) of the steady boundary value problem and the exact asymptotic formulas (solid or dashed lines ). Top row: tilted anchoring ( $\psi_0 = \frac{\pi}{6}$ ) with  $\epsilon = 0.05$  and  $Er = 1$ . Middle row: parallel anchoring ( $\psi_0 = 0$ ) with  $\epsilon = 0.1$  and  $Er = 1$ . Bottom row: normal anchoring ( $\psi_0 = \frac{\pi}{2}$ ) with  $\epsilon = 0.1$  and  $Er = 1$ . In all figures, circles and solid lines use the left (vertical) axis; diamonds and dashed lines use the right axis.

shows the maximum scalar conductivity enhancement ( $\epsilon_{\max}$ ) across the gap for three different anchoring conditions. The top row corresponds to the aspect ratio  $r = 100$  whereas for the bottom row  $r = 3$ . It is apparent that one can achieve different effective conductivity enhancements across the gap by tuning anchoring conditions. The nematogen aspect ratio effect is also significant from this figure. The larger the aspect ratio, the more enhancement in effective conductivity.

It is also interesting to note that the shape of the solution for tangential anchoring is sensitive to the value of aspect ratio. In Figure 6 we plot the maximum effective conductivity enhancement and anisotropy versus Poiseuille flow rate (Figure 6a and

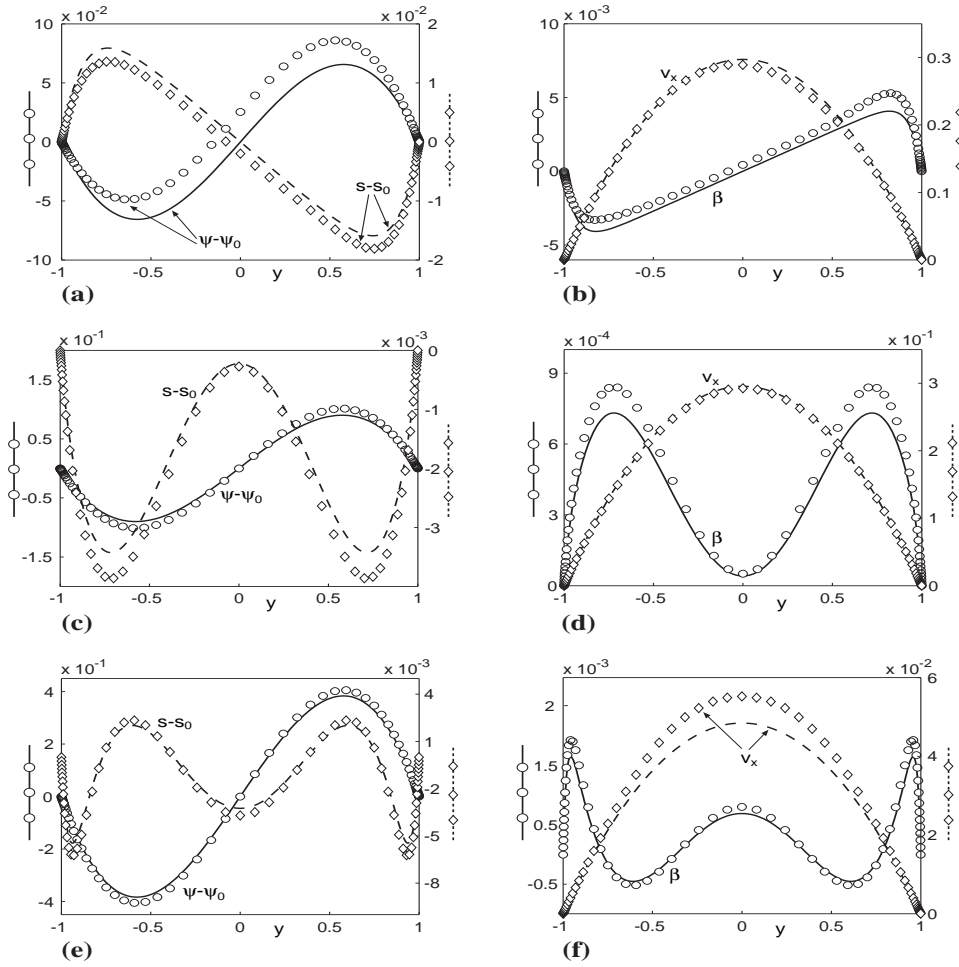


FIGURE 3. Comparison of the numerical solutions (circles or triangles) of the steady boundary value problem and the exact asymptotic formulas (solid or dashed lines). Top row: tilted anchoring ( $\psi_0 = \frac{\pi}{6}$ ) with  $\epsilon = 0.5$  and  $Er = 1$ . Middle row: parallel anchoring ( $\psi_0 = 0$ ) with  $\epsilon = 0.3$  and  $Er = 10$ . Bottom row: normal anchoring ( $\psi_0 = \frac{\pi}{2}$ ) with  $\epsilon = 0.3$  and  $Er = 10$ .

c) and volume fraction (Figure 6b and d) for three different anchoring conditions. The parameters used here are  $r = 100$  and  $Er = 1$ . In Figure 6a and c, the volume fraction is fixed to be  $\theta_2 = 0.0236$  and we vary the Poiseuille flow rate. In this case, tilted anchoring gives the largest conductivity enhancement and anisotropy. In Figure 6b and d, the flow rate  $\epsilon$  is fixed to be 0.1 and we vary the volume fraction  $\theta_2$ . It turns out that the conductivity enhancement and anisotropy are both increasing functions of  $\theta_2$  and insensitive to anchoring conditions.

## 6. Conclusions

We have studied the structure scaling properties of nematic liquid crystal polymers under pressure-driven Poiseuille flow both analytically and numerically. A

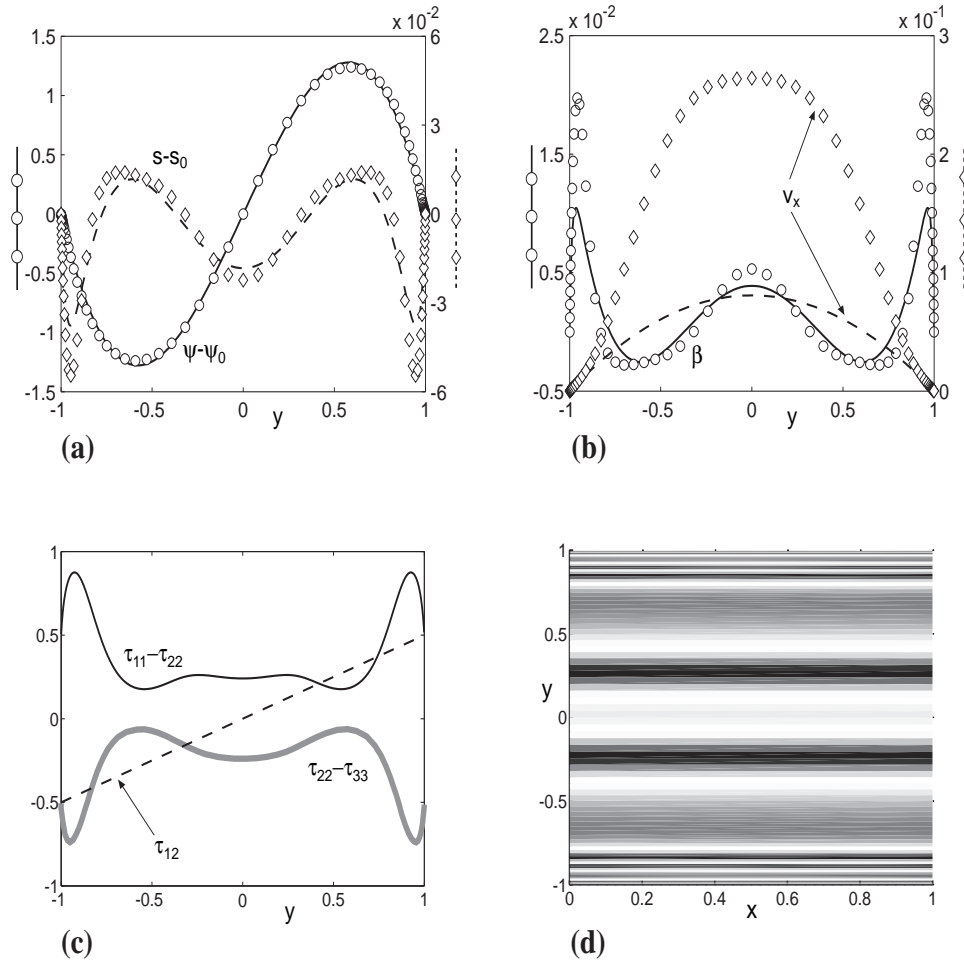


FIGURE 4. Top row: Comparison of the numerical solutions (circles or diamonds) of the steady boundary value problem and the exact asymptotic formulas (solid or dashed lines) for normal anchoring ( $\psi_0 = \pi/2$ ) with  $\epsilon = 0.5$  and  $Er = 20$ . Bottom row: Rheological structure profiles associated with the numerical results of the top row. Here we provide the first ( $N_1 = \tau_{11} - \tau_{22}$ ) and second ( $N_2 = \tau_{22} - \tau_{33}$ ) normal stress differences, the shear stress ( $\tau_{12}$ ), and the light scattering intensity function ([28]),  $I = I_0 \sin^2(2\pi a_1 s)$ , across the plate gap, where  $a_1$  is the ratio of the sample thickness to the wavelength of incident light. The normalized birefringence  $s$  measures the difference between orientation along the flow direction and along the vorticity axis.

rich phenomenology is apparent because of the coupling between the rod ensemble (through excluded volume and distortional elasticity) and the flow field. When the normalized pressure gradient  $\epsilon$  and the scaled Ericksen number  $\epsilon \cdot Er$  are both small, the mesoscopic Doi-Marrucci-Greco model predicts: an  $Er^{-1/2}$  scaling associated with boundary layer modes residing only in the order parameters; and, an  $Er^{-1}$

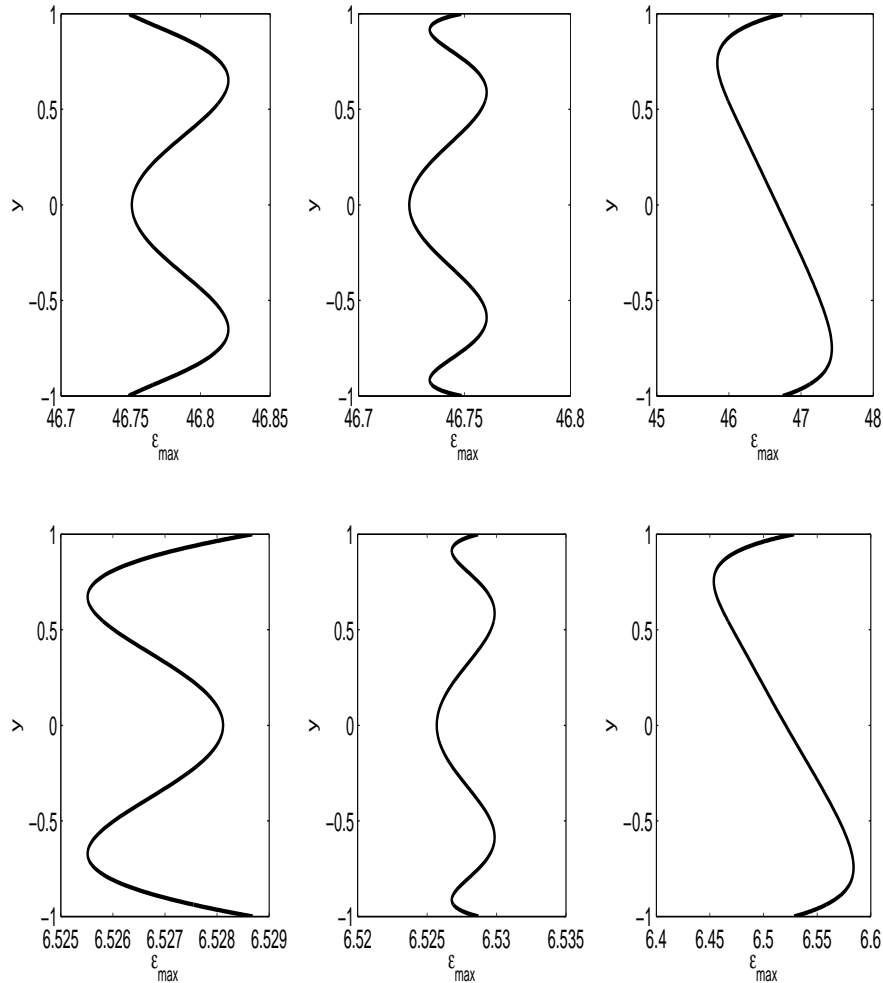


FIGURE 5. Effective conductivity enhancements for 3 different anchoring conditions. Top row:  $r = 100$ ; Bottom row:  $r = 3$ . First column: parallel anchoring; Second column: normal anchoring; Third column: titled anchoring ( $\psi_0 = \frac{\pi}{6}$ ). Here  $\epsilon = 0.5$ ,  $Er = 1$ .

mean scaling law across the rectangular pipe residing in the principal axes of orientation. The self-consistent, leading order, flow velocity is a parabolic Poiseuille flow, attenuated by an explicit prefactor which accounts for the stored energy in the rod dispersion. Anchoring conditions play an important role in the amplitude response of order parameters, which describe the relative focusing or defocusing of the rod ensemble distribution function.

This paper presents a combined approach to understanding flow-induced behavior of rod-like macromolecular dispersions, namely blending modeling, asymptotic analysis, homogenization theory, numerical analysis, and scientific computation. This is, however, just the beginning in an overall strategy to design nano-composite materials from the bottom up. The ideal strategy consists of a control wrapper code, where one is specifying performance features such as current distributions across

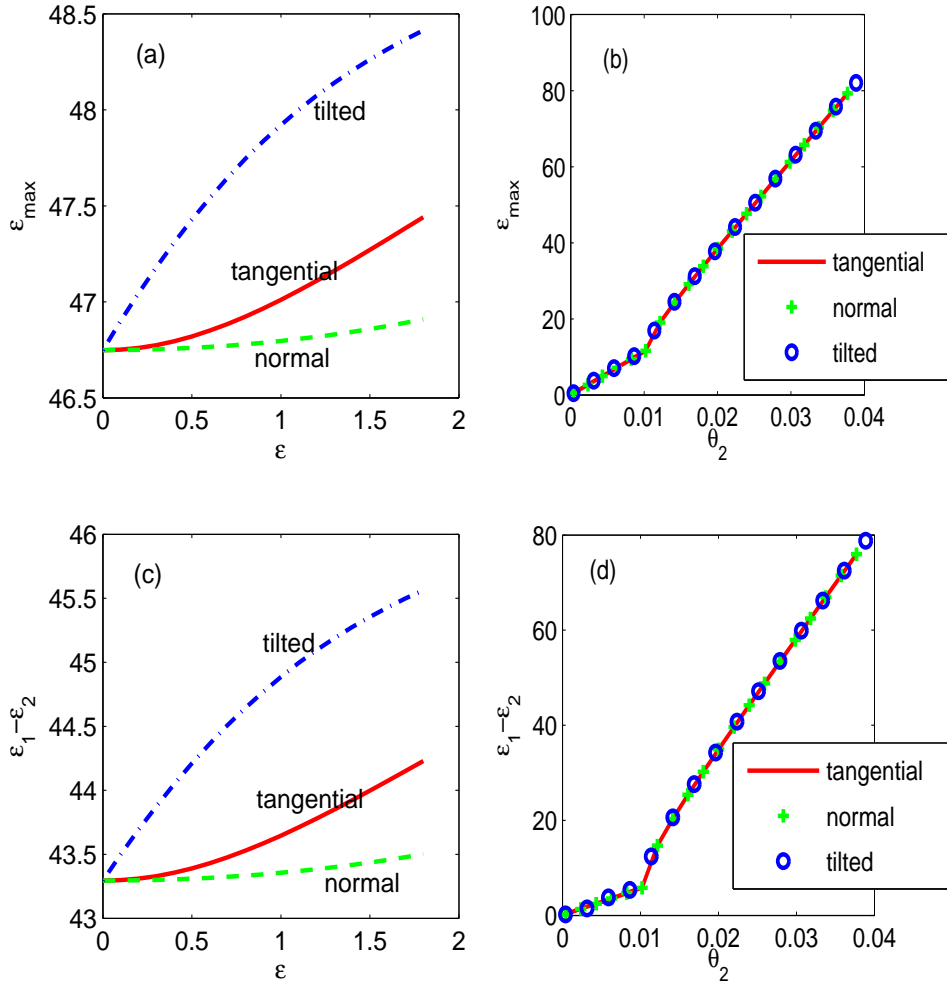


FIGURE 6. Effective conductivity enhancement and anisotropy versus Poiseuille flow rate  $\epsilon$  (a and c) or volume fraction  $\theta_2$  (b and d) for 3 different anchoring conditions.

a material during operating conditions. Using composition information, processing controls, and effective property characterizations, the challenge is to be able to modify composition and processing controls to achieve a specified performance target. It is this challenge that we have only begun to put into a framework, and where the guidance of modern applied mathematics can play a critical role. This paper is dedicated to Max Gunzburger, whose work and consultation over the years has inspired our group to envision such a control strategy in the first place, and whose contributions will be a key to our anticipated success.

**Acknowledgments**

Effort sponsored by the Air Force Office of Scientific Research, Air Force Materials Command, USAF, under grant number FA9550-05-0008, the National Science Foundation through grant DMS-0308019, the Army Research Office, under grant number W911 NF-04-D-0004, and the NASA University Research, Engineering and

Technology Institute on Bio inspired Materials (BIMat) under award No. NCC-1-02037, are gratefully acknowledged. HZ's work is supported in part by the Naval Postgraduate School Research Initiation Program.

## References

- [1] Beris, A.N., Edwards, B.J., **Thermodynamics of Flowing Systems with Internal Microstructure**, Oxford Science Publications (1994).
- [2] Carlsson, T., "Unit-sphere description of nematic flows," *Physical Review A* **34** (4), 3393-3404 (1986).
- [3] Cui, Z., Forest, M.G., Wang, Q., and Zhou, H., "On weak plane Couette and Poiseuille flows of rigid rod and platelet ensembles," to appear in *SIAM J. Appl. Math.* (2006).
- [4] de Andrade Lima, L. R. P., and Rey, A.D., "Linear and nonlinear viscoelasticity of discotic nematics under transient Poiseuille flows," *J. Rheol.* **47**, 1261-1282 (2003a).
- [5] de Andrade Lima, L. R. P., and Rey, A.D., "Poiseuille flow of Leslie-Ericksen discotic liquid crystals: solution multiplicity, multistability, and non-Newtonian rheology," *J. Non-Newtonian Fluid Mech.* **110**, 103-142 (2003b).
- [6] de Andrade Lima, L. R. P., and Rey, A.D., "Superposition and universality in the linear viscoelasticity of Leslie-Ericksen liquid crystals," *J. Rheol.* **48**, 1067-1084 (2004).
- [7] de Gennes, P.G., **The Physics of Liquid Crystals**, Clarendon Press (1974).
- [8] de Gennes, P.G., Prost, J., **The Physics of Liquid Crystals**, Oxford University Press (1993).
- [9] Denniston, C., Orlandini, E., and Yeomans, J.M., "Simulations of liquid crystals in Poiseuille flow," *Computational and Theoretical Polymer Science* **11**, 389-395 (2001).
- [10] Doi, M., Edwards, S.F., **The Theory of Polymer Dynamics**, Oxford U. Press (Clarendon), London-New York (1986).
- [11] Donald, A. M., and Windle, A. H., **Liquid Crystalline Polymers**, Cambridge Solid State Science Series, Cambridge University Press (1992).
- [12] Ericksen, J. L., "Liquid crystals with variable degree of orientation," *Arch. Ration. Mech.* **113**, 97-120 (1991).
- [13] Feng, J., Sgalari, G., and Leal, L.G., "A theory for flowing nematic polymers with orientational distortion," *J. Rheol.* **44**, 1085-1101 (2000).
- [14] Forest, M.G. and Wang, Q., "Monodomain response of finite-aspect-ratio macromolecules in shear and related linear flows," *Rheol. Acta*, **42**, 20-46 (2003).
- [15] Forest, M.G., Wang, Q. and Zhou, H., "Exact banded patterns from a Doi-Marrucci-Greco model of nematic liquid crystal polymers," *Physical Review E* **61** (6), 6655-6662 (2000).
- [16] Forest, M.G., Wang, Q., and Zhou, H., "Methods for the exact construction of mesoscale spatial structures in liquid crystal polymers", *Physica D*, **152-153**, 288-309 (2001).
- [17] Forest, M.G., Wang, Q., Zhou, H., and Zhou, R., "Structure scaling properties of confined nematic polymers in plane Couette cells: The weak flow limit," *J. Rheol.*, **48**, 175-192 (2004).
- [18] Forest, M.G., Zheng, X., Zhou, R., Wang, and R., Lipton, "Anisotropy and dynamic ranges in effective properties of sheared nematic polymer nano-composites," *Adv. Func. Mat.*, **15**, 2029-2035 (2005).
- [19] Hinch E.J., and Leal, L.G., "The effect of Brownian motion on the rheological properties of a suspension of non-spherical particles", *J. Fluid Mech.* **52**(4), 683-712 (1972).
- [20] Kuzuu, N., Doi, M.J., "Constitutive equation for nematic liquid crystals under weak velocity gradient derived from a molecular kinetic equation," *Phys. Soc. Japan* **52**(10), 3486-3494 (1983).
- [21] Kuzuu, N., Doi, M.J., "Constitutive equation for nematic liquid crystals under weak velocity gradient derived from a molecular kinetic equation, II. Leslie coefficients for rodlike polymers," *Phys. Soc. Japan* **53**, 1031-1040 (1984).
- [22] Kupferman, R., Kawaguchi, M. and Denn, M.M., "Emergence of structure in a model of liquid crystalline polymers with elastic coupling," *J. Non-Newt. Fluid Mech.* **91**, 255-271 (2000).
- [23] Larson, R.G., **The Structure and Rheology of Complex Fluids**, Oxford University Press (1999).
- [24] Manneville, P., "The transition to turbulence in nematic liquid crystals: Part 1, general review. Part 2, on the transition via tumbling," *Mol. Cryst. Liq. Cryst.* **70**, 223-250 (1981).
- [25] Marrucci, G., "Tumbling regime of liquid-crystalline polymers," *Macromolecules*, **24**, 4176-4182 (1991).

- [26] Marrucci, G. and Greco, F., "The elastic constants of Maier-Saupe rodlike molecular nematics," *Mol. Cryst. Liq. Cryst.* **206**, 17-30 (1991).
- [27] Marrucci, G. and Greco, F., "Flow behavior of liquid crystalline polymers," *Adv. Chem. Phys.*, Vol 86, edited by I. Prigogine and S. Rice (1993).
- [28] Mather, P.T., Romo-Uribe, A., Han, C.D. and Kim, S.S., "Rheo-optical evidence of a flow-induced isotropic-nematic transition in a thermotropic liquid-crystalline polymer," *Macromolecules* **30**(25), 7977-7989 (1997).
- [29] Rey, A.D. and Denn, M.M., "Dynamical phenomena in liquid-crystalline materials", *Annual Rev. Fluid Mech.* **34**, 233-266 (2002).
- [30] Tan, Z. and Berry, G.C., "Studies on the texture of nematic solutions of rodlike polymers, 3. Rheo-optical and rheological behavior in shear," *J. Rheol.* **47**(1), 73-104 (2003).
- [31] Toth, P.A., Krekhov, L., Kramer, L., and Peinke, J., "Orientational transition in nematic liquid crystals under oscillatory Poiseuille flow," *Europhys. Lett.* **51**, 48-54 (2000).
- [32] Zheng, X., Forest, M. G., Lipton, R., Zhou, R. and Wang, Q., "Exact scaling laws for electrical conductivity properties of nematic polymer nano-composite monodomains," *Advanced Functional Materials* **15**, 627-638 (2005).
- [33] Zhou, H., Forest, M. G., Zheng, X., Wang, Q., and Lipton, L., "Extension-enhanced conductivity of liquid crystalline polymer nano-composites," *Macromolecular Symposia*, **228**, 81-89 (2005).
- [34] Zhou, H. and Forest, M. G., "Anchoring distortions coupled with plane Couette & Poiseuille flows of nematic polymers in viscous solvents: morphology in molecular orientation, stress & flow," *Discrete and Continuous Dynamical Systems*, **6**(2), 407-425 (2006).

Department of Applied Mathematics, Naval Postgraduate School, Monterey, CA 93943-5216, USA

*E-mail:* hzhou@nps.navy.mil

Department of Mathematics, University of North Carolina at Chapel Hill, Chapel Hill, NC 27599-3250, USA

*E-mail:* forest@amath.unc.edu